Strong Interplay between Sodium and Oxygen in Kesterite Absorbers: Complex Formation, Incorporation, and Tailoring Depth Distributions

Sigbjørn Grini, Kostiantyn V. Sopiha, Nils Ross, Xin Liu, Tor S. Bjørheim, Charlotte Platzer-Björkman, Clas Persson, and Lasse Vines*

Sodium and oxygen are prevalent impurities in kesterite solar cells. Both elements are known to strongly impact performance of the kesterite devices and can be connected to efficiency improvements seen after heat treatments. The sodium distribution in the kesterite absorber is commonly reported, whereas the oxygen distribution has received less attention. Here, a direct relationship between sodium and oxygen in kesterite absorbers is established using secondary ion mass spectrometry and explained by defect analyses within the density functional theory. The calculations reveal a binding energy of 0.76 eV between the substitutional defects Na_{Cu} and O_S in the nearest neighbor configuration, indicating an abundance of Na—O complexes in kesterite absorbers at relevant temperatures. Oxygen incorporation is studied by introducing isotopic ^{18}O at different stages of the Cu_2ZnSnS_4/Mo/soda-lime glass baseline processing. It is observed that oxygen from the Mo back contact and contaminations during the sulfurization are primary contributors to the oxygen distribution. Indeed, unintentional oxygen incorporation leads to immobilization of sodium. This results in a strong correlation between sodium and oxygen, in excellent agreement with the theoretical calculations. Consequently, oxygen availability should be monitored to optimize postdeposition heat treatments to control impurities in kesterite absorbers and ultimately, the solar cell efficiency.

1. Introduction

Earth-abundant kesterite $Cu_2ZnSn(S,Se)_4$ (CZTSSe) is a promising solar cell absorber with a record 12.6% power conversion efficiency (PCE).[1] In recent years, several groups have achieved over 10% efficiency with control over fabrication and doping as key factors.[2–8] However, control over impurities during processing in kesterite and other chalcogenide technologies is challenging. Although the effects of impurities on solar cell device performance have been discussed extensively, a complete understanding of their behavior and impact is still lacking. For chalcogenide thin film solar cells, Na and O are the prevalent impurities,[6,9–13] where both are often found to accumulate at grain boundaries (GBs).[14,15] Importantly, moderate amounts of Na present during fabrication are almost exclusively regarded as beneficial for device performance,[9] whereas the effect of O is more ambiguous. For instance, the champion CZTSSe cell from Wang et al.[1] exhibited low C and O concentrations. Early studies on $Cu(In,Ga)Se_2$ (CIGS), however, implied that an interplay between Na and O affects the PCE because O may passivate Se vacancies at grain boundaries with Na acting as a catalyst.[16–18] Indeed, further studies confirmed that Na and O can coexist on the surface and GBs.[19,20] Moreover, for both CIGS and CZTSSe, postdeposition heat treatments were shown to yield improved device performance.[21] For kesterite solar cells, these treatments have been performed in air, inert atmosphere, and vacuum.[10,22–25] The heat treatments have been observed to change the photoluminescence intensity and peak position,[22,24] the sodium distribution,[10,24] the bandgap,[22,25] surface properties[22] as well as oxidize the surface and grain boundaries.[14,25] Consequently, impurities such as Na and O can be a critical factor influencing the device performance. On one hand, Na incorporation is achieved by using soda-lime glass substrates (SLG) and suppressing other Na sources. On the other hand, O is not as easily controlled since multiple potential sources may exist. For example, commonly used glass substrates, such as SLG, are composed of oxides. Furthermore, the Mo back contact is polycrystalline and usually contains significant amounts of O.[26] Additionally, the precursors may contain O and all process stages are performed in low-to-medium vacuum conditions, under which O may also be present.

In this work, a correlation between Na and O distribution in kesterite absorbers is identified using secondary ion

S. Grini, Dr. X. Liu, Dr. T. S. Bjørheim, Prof. C. Persson, Prof. L. Vines
Department of Physics/Centre for Materials Science and Nanotechnology
University of Oslo
P.O. Box 1048, Blindern N-0316, Oslo, Norway
E-mail: sigbjorn.grini@smn.uio.no
Dr. K. V. Sopiha, Dr. N. Ross, Prof. C. Platzer-Björkman
Ångström Solar Center
Division of Solid State Electronics
Uppsala University
Uppsala 75120, Sweden
The ORCID identification number(s) for the author(s) of this article can be found under https://doi.org/10.1002/aenm.201900740.

DOI: 10.1002/aenm.201900740

mass spectrometry (SIMS) and explained by defect analyses within the density functional theory (DFT), where a model with complex formation and subsequent trapping of Na is proposed. The model is experimentally explored by introducing the less abundant ^{18}O isotope into different stages of the CZTS baseline process. Further, the ^{18}O investigation reveals the sources of O that contribute to the final O distribution observed in the absorber.

2. Results and Discussion

2.1. Interplay between Na and O Impurities in Kesterite Absorbers

Figure 1 shows SIMS depth profiles for two CZTSSe absorbers chosen from our previous study of high-performance devices.[27] The lines represent Na (red) and O (black) distribution in the absorbers which yielded PCEs of 8.5% (solid lines) and 7.2% (dashed lines), respectively. SIMS depth profiles of the constituent elements are shown in Figure S1 (Supporting Information). For both samples, the Na and O profiles are correlated, which is a trend previously observed for CZTSSe and CIGS.[28–30] Interestingly, the correlation persists regardless of the shape of the profile. This is exemplified in Figure 1 for the 7.2% PCE device where an abnormal accumulation for both Na and O is observed at about 500 nm into the sample. The fact that the accumulation is in the middle of the absorber cannot be easily explained by the SIMS intensity only representing GB density.[31] Indeed, none of our scanning electron microscopy cross-section images showed an increase of GB density in this region. To understand the correlation between Na and O in kesterite absorbers at the atomic level, first-principles DFT was employed to study the point defects formed by these impurities in CZTS. The sole defects and possible complexes can be

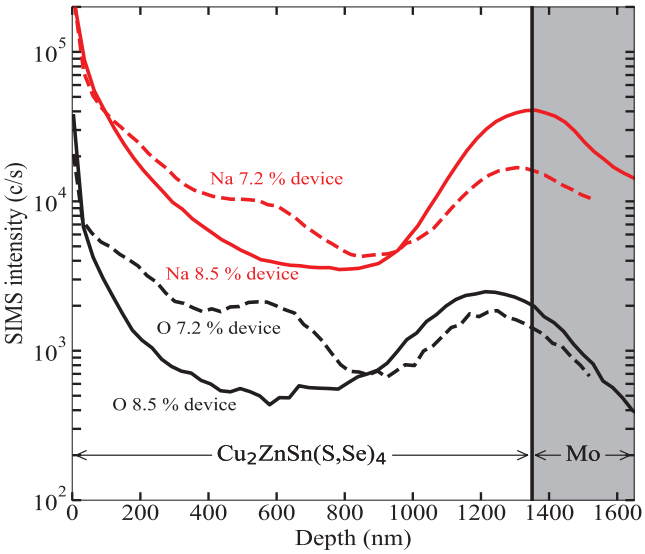

Figure 1. SIMS depth profiles of Na (red lines) and O (black lines) measured on two CZTSSe absorbers where the mean device produced an 8.5% PCE (solid lines) and a 7.2% PCE (dashed lines). The Na and O depth profiles correlate for both samples and represent a trend observed for all our measured kesterite absorbers.

formed in the grain interior, but it is also known that both sodium and oxygen often accumulate at GBs of both CZTS[14,32] and CIGS.[15,33,34] In recent studies, alkali impurities were even shown to segregate at specific GBs,[35] marking a new stage in understanding the impact of Na on polycrystalline Cu-based solar cells. In this work, we analyze defect physics in bulk CZTS, and thus, we do not try to describe more complex situations for GBs.[36–42]

For bulk CZTS, Na-related defects are already relatively well investigated in the literature. It is known that Na prefers to occupy Cu site in CZTS to form Na_{Cu},[43–45] although formation of interstitial Na_i is possible during diffusion.[46,47] The substitutional Na_{Cu} is an isovalent defect, and since the ionic radius of Na is about 0.4 Å larger than that of Cu, it does not yield any local reconstruction of the crystal.[48] These results were confirmed by our calculations. On the other hand, the O impurities have only been addressed by a few first-principles studies,[36,49] which hypothesized the dominant role played by substitutional O_S defect. Conversely, we found that O_S induces a substantial local lattice distortion due to significant differences in both size and electronegativity between the O^{2-} and S^{2-} ions.

While the calculated Cu—S, Zn—S, and Sn—S bond lengths in CZTS are 2.32, 2.37, and 2.47 Å, the Cu(2a)—O, Cu(2c)—O, Zn—O, and Sn—O distances for the O_S defect are 3.23, 2.18, 1.99, and 2.02 Å, respectively. This change in the coordination for O_S can be interpreted as breaking the Cu(2a)—O and shortening the remaining bonds by 0.14–0.45 Å, in accordance with a general tendency for stabilizing shorter bonds between atoms with smaller ionic radii.[48] These optimized configurations for substitutional defects were further used as reference systems to compute binding energy between Na_{Cu} and O_S.

Apart from the isolated defects, Na and O impurities in CZTS may interact through formation of defect complexes. Now, consider that the NaO complex is formed by Na_{Cu} and O_S. The binding energy for such defect complex can be computed as

$$E_b = E_{tot}(Na) + E_{tot}(O) - E_{tot}(Na+O) - E_{tot}(\text{pristine}) \quad (1)$$

where $E_{tot}(Na)$, $E_{tot}(O)$, $E_{tot}(Na+O)$, and $E_{tot}(\text{pristine})$ are the total energies of CZTS supercells containing isolated Na_{Cu}, isolated O_S, both Na_{Cu} and O_S, and pristine supercell, respectively. Similar expressions can also be written for the larger Na—O complexes using the supercell with NaO complex as a reference system, hence, the binding energy computed in such a way defines strength of the subsequent Na—O bonds. It was found that Na—O binding energy of the NaO complex strongly depends on distance between the defects, as shown in **Figure 2**a.

The highest computed binding energy of 0.76 eV corresponds to the NaO complex where Na_{Cu} and O_S are nearest neighbors. This binding energy is remarkably high considering that both Na_{Cu} and O_S are isovalent substitutional defects. In case of the Na_2O complex, binding energy for the second Na_{Cu} with the existing NaO complex is 0.56 eV (i.e., total binding energy of 0.76 + 0.56 = 1.32 eV), which is comparable to that for the NaO complex. Further, since Na diffusion in CZTS can be mediated by the interstitial defects,[46] binding energy was also computed for interstitial Na_i and substitutional O_S, demonstrating qualitatively similar results. In fact, the most stable complex formed by neutral Na_i and O_S has binding energy of 1.19 eV, which is even higher than that for Na_{Cu} and O_S. More

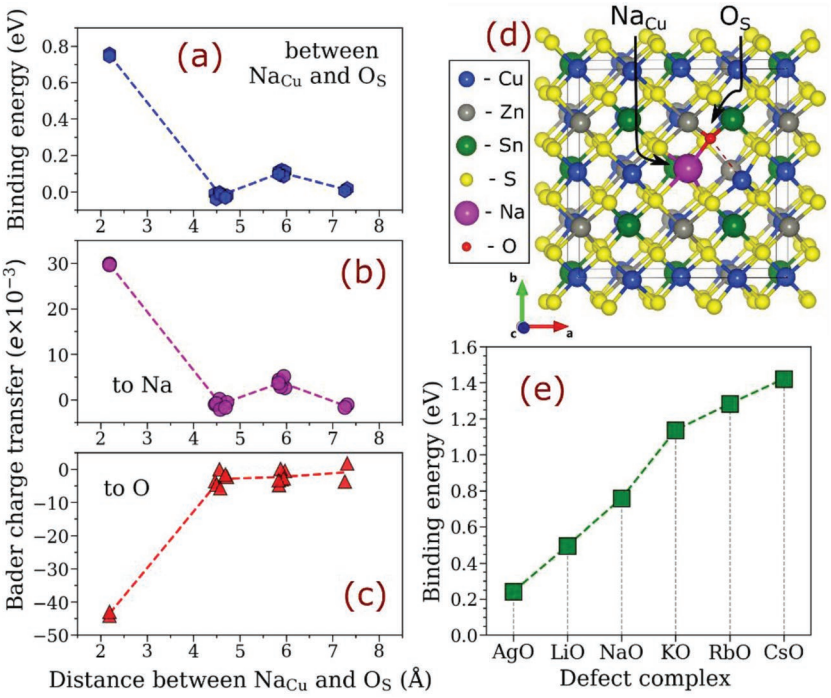

Figure 2. First-principles analysis of interaction between Na_{Cu} and O_S defects in CZTS. a) Binding energy of Na_{Cu} and O_S in 64-atom supercell versus distance between them. b,c) Bader charge transfer to Na and to O atoms versus distance between them; the separated defects in 64-atom CZTS supercells were used as reference systems for the binding energy and Bader charge transfer calculations. d) Structure of the most stable nearest-neighbor NaO complex; the broken Cu—O bond is illustrated by the red dashed line; the corresponding .CIF file is given in the Supporting Information. e) Binding energy for complexes formed between O_S and different isovalent substitutional defects on the Cu site; only the most stable configurations of the complexes are presented. The dashed lines in all graphs are to guide the eye.

detailed analysis of the defect interaction in the Na_2O complex and for Na_i with O_S is given in the Supporting Information. This strong tendency for binding suggests that Na atoms introduced into O-containing CZTS grains can be kinetically trapped by forming the nearest neighbor complexes.

To explain the origin of the remarkably strong binding, we analyze in detail the most stable configuration of the NaO complex between Na_{Cu} and O_S (see Figure 2d). First, it is notable that the Na—O bond of 2.19 Å is very close to the corresponding Cu—O bond for the isolated O_S defect (2.18 Å), suggesting relatively small contribution of the lattice relaxation. Indeed, we found that binding energy of NaO complex where both Na_{Cu} and O_S occupy the ideal lattice sites (without atomic relaxation) is 0.67 eV. Second, effective (Bader) charges were calculated for Na and O with respect to the distance between them, as shown in Figure 2b,c. Evidently, the charges transferred to Na and O correlate with the binding energy, that is, charge transfers are significant in the nearest neighbor configurations only. This behavior suggests that binding in the complexes is determined by ionicity of the Na—O bond and justifies why the binding energy causing formation of the second Na—O bond in Na_2O complex (0.56 eV) is almost as high as that for NaO (0.76 eV). Third, the binding energies for five other isovalent XO (X = Ag, Li, K, Rb, Cs) defect complexes were also computed. As can be observed in Figure 2e, the binding energy correlates with electronegativity of the X atom, affirming that bonding between Na and O in bulk CZTS is indeed determined by the ionic bond, and thus, qualitatively similar interaction between the defects at the GBs can be expected. Fourth, the binding energies were calculated for the complexes formed by O_S and interstitial X_i defect (X = Ag, Li, Na, K, Rb, and Cs), as shown in Figure S3 (Supporting Information), further evincing that the interaction between the alkali elements and oxygen is driven by the ionic bonding. These results corroborate the conclusion that Na and O concentrations in CZTS are indeed correlated, as seen in the SIMS depth profiles in Figure 1, and that the origin of this correlation is indeed Na—O defect complexes.

Although the calculations show a clear tendency for binding between Na_{Cu} and O_S in CZTS, the binding energy alone does not guarantee the formation of the complexes at the processing and/or operating temperatures. The concentration of AB complexes at temperature T can be estimated from the law of mass action as

$$C_{AB} = C_A \times C_B \times GF \times \exp\left(E_b/kT\right) \quad (2)$$

where C_A and C_B are concentrations of isolated A and B defects, respectively; GF is a factor accounting for both the lattice symmetry and the complex geometry.[50] The law of mass action can be applied to all other complexes as well and should be collectively satisfied for all defects in equilibrium. Equation (2) is strictly valid in the dilute limit, but for this study it would be a reasonable approximation for the defect concentrations below 1 at% because the Na—O interaction is very short-ranged and the change in entropy is insufficient to outcompete the strong Na—O bond. In our CZTS samples, the total concentrations of Na and O impurities were estimated using elastic recoil detection analysis (ERDA) to be 0.8 and 0.5 at%, respectively. Based on this stoichiometry, one could expect NaO and Na_2O to be dominant. Assuming no influx of the impurities upon heating, their total concentrations are constrained as $C_A^{tot} = C_A + C_{AB} + 2C_{A_2B}$ and $C_B^{tot} = C_B + C_{AB} + C_{A_2B}$. Hence, by solving the system of equations with E_b = 0.76 eV and GF = 8 representing the NaO complex and E_b = 0.56 eV and GF = 4 for the Na_2O complex in CZTS, the temperature dependence for the defect concentrations can be obtained, as shown in **Figure 3**a (solid lines). As one can see, these high binding energies ensure the formation of both complexes at all temperatures of CZTS baseline processing (below 600 °C). In a wider range of compositions, however, the dominant type of complexes depends on the ratio of the defects introduced, as shown in Figure 3b. Thus, when concentration of O is closer to that of Na, formation of NaO would be dominant (e.g. dotted lines in Figure 3a). Contrary, when concentration of Na is about twice that of O, predominant formation of Na_2O can be expected. In the intermediate regime, both types of complexes would coexist. These results as such demonstrate that Na and

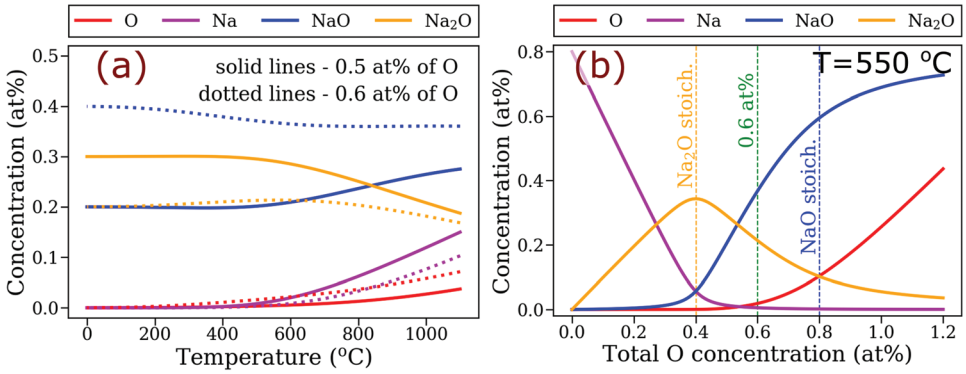

Figure 3. Estimated concentrations of Na_{Cu}, O_S, NaO, and Na_2O complexes a) with respect to temperature for CZTS containing 0.8 at% of Na with 0.5 at% (solid lines) and 0.6 at% (dotted lines) of O, and b) with respect to total O concentration at 550 °C and 0.8 at% of Na.

O impurities primarily coexist in the form of defect complexes throughout the typical temperature interval adopted in CZTS processing. At the same time, they do not exclude the possibility of clustering between the NaO complexes forming even larger complexes. Most importantly, however, the tendency for binding between Na and O in CZTS ensures that these impurities do interplay and cluster owing to the strong ionic Na—O bonding, and therefore, must be considered together for developing high-performance CZTS solar cells.

To control the formation of Na—O complexes, however, the origins of Na and O incorporation in kesterite processing must be identified. While Na is incorporated from Na_2O present in SLG,[51] concurrent diffusion of O from the substrate is also possible, even though the diffusivities of alkali elements are much higher in SLG compared to that of O.[52] Additionally and different to Na, O in kesterite absorbers has several additional potential sources: outdiffusion from the Mo back contact, from the precursors as well as from the air during and after processing.

2.2. Evaluation of Sources of O in Kesterite Processing by Isotopic ^{18}O Diffusion

To further study the relationship between Na and O in kesterite absorbers, controlled O incorporation during processing is needed. To evaluate possible sources of O, isotope ^{18}O was introduced at different stages of the CZTS baseline processing by heat treatments in an ^{18}O-rich atmosphere ([^{18}O]: 97.1%, [^{16}O]: 2.9%) at 100, 200, 300, and 400 °C for 30 min (hereafter called ^{18}O anneal). The heat treatments were performed (①) on the SLG substrate, (②) after the Mo sputtering, (③) after the CZTS precursor sputtering, and (④) after the sulfurization, as shown in **Figure 4**. The SLG was only heat treated at 400 °C since no significant diffusion was expected at lower temperatures.[52] The isotopic ratio $C_{^{18}O}$ = [^{18}O]/([^{16}O] + [^{18}O]) versus depth after the ^{18}O anneals and for untreated CZTS absorbers measured with SIMS are shown in **Figure 5**. The cation ratios, processing steps, and annealing conditions are summarized in **Table 1**.

In Figure 5a, the depth profile for "SLG 400 °C" (①, brown dashed line) has increased isotopic ratio in the Mo back contact. The increased ^{18}O concentration demonstrates that O can diffuse from the SLG into the Mo layer during the CZTS processing. However, since the isotopic ratio in the treated and untreated CZTS layers are at the same level, SLG can be excluded from the list of potential sources of O in CZTS for baseline processing conditions.

Additionally, Figure 5a shows that ^{18}O diffuses into the Mo back contact during the ^{18}O anneal (②, solid lines). The

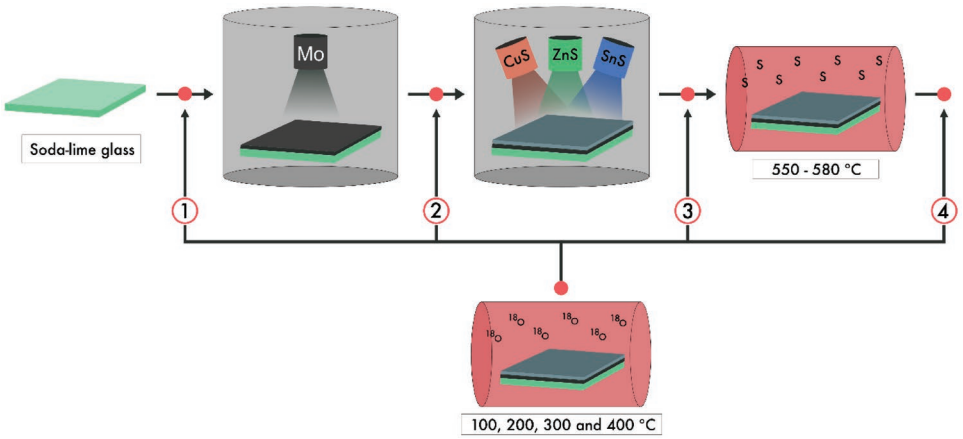

Figure 4. ^{18}O introduction into different stages of the CZTS processing; (①) on the soda-lime glass substrate, (②) after the Mo sputtering, (③) after the CZTS precursor (CuS, ZnS, and SnS) sputtering, and (④) after the sulfurization.

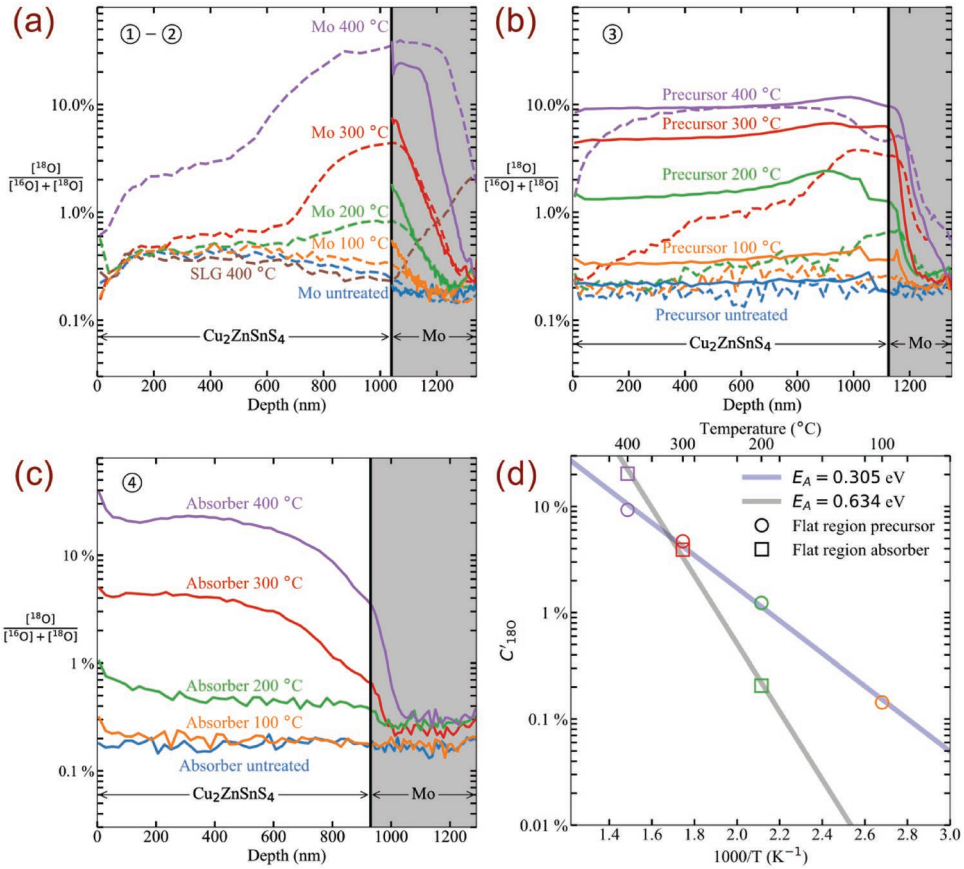

Figure 5. The isotopic ratio $C_{^{18}O} = [^{18}O]/([^{16}O] + [^{18}O])$ measured with SIMS at different stages of the CZTS baseline process. The solid lines in (a)–(c) represent depth profiles measured after a heat treatment in an ^{18}O-rich atmosphere for 30 min. The dashed lines in (a) and (b) represent depth profiles after the samples have been processed to CZTS absorbers. "Untreated" indicates a reference sample not heat treated in the ^{18}O-rich atmosphere but processed in the same conditions otherwise. The number(s) in the upper left corner refers to the process stages shown in Figure 4. Thus, the heat treatment in the ^{18}O-rich atmosphere is performed a) before and after the Mo sputtering, b) after the CZTS precursor sputtering, and c) after the sulfurization. d) Arrhenius behavior between the ^{18}O fraction corrected for the isotopic background level of ^{18}O and for the isotope fraction in an ^{18}O-rich atmosphere, $C'_{^{18}O}$, for the ^{18}O inclusion into the precursor and the CZTS absorber. The circles and squares represent average for the flat regions in the depth profiles of the ^{18}O annealed precursors and absorbers, respectively.

isotopic ratio increases with annealing temperature up to 20% for "Mo 400 °C". During the precursor deposition and sulfurization, ^{18}O from the Mo back contact diffuses into the CZTS layer (dashed lines), indicating that O from the Mo back contact inevitably ends up in the CZTS layer. The isotopic ratio is higher near the Mo back contact, suggesting that O diffusion in the CZTS layer is not fast enough to uniformly distribute O throughout its thickness. From 100 nm to about 600 nm from the surface, the isotopic ratio is nearly constant, while the isotopic ratio approaches the background natural abundance level, $C_{bg} = 0.2\%$, near the surface. Surprisingly, a small increase in the isotopic ratio above the background level is found in all profiles, including that for the untreated sample. This feature can be attributed to a minor ^{18}O exchange effect caused by keeping all the samples in the same graphite box during the sulfurization. Indeed, a follow-up control experiment for an untreated sample in a separate box (not shown) revealed only the natural abundance of ^{18}O, confirming the exchange mechanism causing the abnormality in the isotopic profiles.

After the ^{18}O anneal (②) of "Mo 400 °C", the Mo layer turned from metallic to dark red and X-ray diffraction data unveiled the presence of MoO_2 (Figure S5, Supporting Information). The formation of oxide phase should not affect the isotopic ratio, even though it causes an increase in SIMS intensity for both ^{16}O and ^{18}O due to higher ionization yield in MoO_2 compared to that of Mo. Here, it should be noted that high SIMS intensities require a faraday cup detector to be used to protect the normal electron multiplier, which yields an uncertainty in the isotopic ratio. This effect may explain the higher ratio measured after the precursor deposition and sulfurization for "Mo 400 °C" (Figure 5a, purple dashed line).

In this work, the CZTS baseline processing employs CuS, ZnS, and SnS sputtering targets with 99.99% purity in chamber with an Ar (99.9995% purity) background pressure of 666 Pa. Despite the high purities, noticeable O concentrations are detected by SIMS in the samples prior to sulfurization (not shown). Hence, ^{18}O anneals were performed before the sulfurization to study whether the O from the precursors eventually ends up in the CZTS absorber.

Table 1. The sample names, the cation ratios, and when the samples were annealed in an ^{18}O-rich atmosphere.

Sample name	Cation ratios		^{18}O annealed
	[Cu]/[Sn]	[Zn]/([Cu]+[Sn])	
SLG 400 °C	1.78 ± 0.02	0.41 ± 0.02	400 °C on the soda-lime glass substrate
Mo untreated	1.78 ± 0.02	0.41 ± 0.02	–
Mo 100 °C	1.78 ± 0.02	0.41 ± 0.02	100 °C after Mo sputtering
Mo 200 °C	1.78 ± 0.02	0.41 ± 0.02	200 °C after Mo sputtering
Mo 300 °C	1.78 ± 0.02	0.41 ± 0.02	300 °C after Mo sputtering
Mo 400 °C	1.78 ± 0.02	0.41 ± 0.02	400 °C after Mo sputtering
Precursor untreated	1.95 ± 0.02	0.38 ± 0.02	–
Precursor 100 °C	1.95 ± 0.02	0.38 ± 0.02	100 °C after cosputtering of precursors
Precursor 200 °C	1.95 ± 0.02	0.38 ± 0.02	200 °C after cosputtering of precursors
Precursor 300 °C	1.95 ± 0.02	0.38 ± 0.02	300 °C after cosputtering of precursors
Precursor 400 °C	1.95 ± 0.02	0.38 ± 0.02	400 °C after cosputtering of precursors
Absorber untreated	1.83 ± 0.02	0.34 ± 0.02	–
Absorber 100 °C	1.83 ± 0.02	0.34 ± 0.02	100 °C after sulfurization
Absorber 200 °C	1.83 ± 0.02	0.34 ± 0.02	200 °C after sulfurization
Absorber 300 °C	1.83 ± 0.02	0.34 ± 0.02	300 °C after sulfurization
Absorber 400 °C	1.83 ± 0.02	0.34 ± 0.02	400 °C after sulfurization

Figure 5b illustrates that the isotopic ratio in the samples after the ^{18}O anneals (③) is roughly constant throughout the precursor layer followed by a decrease in the Mo layer (solid lines). Additionally, the isotopic ratio increases with annealing temperature. After the sulfurization, the isotopic ratio in the CZTS layer for "Precursor 300 °C" and "Precursor 200 °C" drop significantly. The reductions are from about 4 to 1% for "Precursor 300 °C" and from about 1.4 to 0.3% for "Precursor 200 °C". Interestingly, these depth profiles in the CZTS layer resemble those after ^{18}O was introduced in the Mo layer (Figure 5a). Consequently, the isotopic profiles are likely to be formed by ^{18}O diffusing through the CZTS precursor and into the Mo during the ^{18}O anneal (solid lines in the Mo region).

Conversely, for "Precursor 400 °C", the majority of the ^{18}O remains in the CZTS layer. The total O concentration is also higher for this sample (not shown), which indicates that the precursor oxidizes to an extent such that outdiffusion during the sulfurization process is prevented. An effort was made to fabricate devices from the precursor-annealed samples. However, most of them flaked off during the chemical bath deposition. Interestingly though, "Precursor untreated" and "Precursor 400 °C" flaked off the least. Some small subcells were fabricated from these films, but their PCE was low presumably due to nonideal cation stoichiometry and no difference in PCE was observed between the untreated and heat-treated samples. For close to ideal stoichiometric cation ratios, one could expect that air anneal of the precursors at 400 °C increases the O concentration in the CZTS layer and may affect the solar cell performance. Ultimately, apart from "Precursor 400 °C", the O from the precursor accounts for only a miniscule part of the O concentration found in the CZTS absorber.

To investigate how likely O is to be introduced into crystallized absorbers, ^{18}O anneals were also performed after the sulfurization (④). SIMS depth profiles in Figure 5c show that after ^{18}O anneals above 100 °C, ^{18}O diffused into the CZTS layer and the Mo back contact. In the CZTS layer, the isotopic ratio is nearly constant for the "Absorber 200 °C", while for higher temperatures the isotopic ratio starts to decline toward the Mo layer at a depth of about 650 nm.

Interestingly, the ^{18}O anneals starting from 200 °C for the absorbers (④) and from 100 °C for the precursors (③) yielded a depth profile with distinct regions of constant isotopic ratio. These constant profiles define regions where shapes of the ^{16}O and ^{18}O concentration profiles are identical. This correlation is expected from a direct exchange between ^{18}O and ^{16}O during the ^{18}O anneal. Provided O diffuses fast in CZTS, the incorporation of O from the atmosphere might be limited by the rate of surface exchange reactions. Adapting the procedure used for studying $^{18}O/^{16}O$ isotopic exchange and O transport in oxides,[53] the isotopic ratio can be corrected for the C_{bg} and for the ^{18}O isotopic ratio in the ^{18}O-rich atmosphere, C_g. This parameter is defined here as

$$C'_{^{18}O} = \frac{C_{^{18}O} - C_{bg}}{C_g - C_{bg}} \tag{3}$$

From the flat regions in the depth profiles in Figure 5b,c, the $C'_{^{18}O}$ can be calculated and plotted with respect to the annealing temperature, as shown in Figure 5d. As one can see, the ^{18}O isotopic ratio follows an Arrhenius behavior for both the precursor and the absorber. The activation energy for O incorporation into the precursor is half of that into the absorber. Indeed, the Arrhenius behavior indicates a negligible (<0.01%) increase in $C'_{^{18}O}$ during the 100 °C anneal of the absorber, which is less than the natural abundance and is not detectable with SIMS. Consequently, it can be concluded that prolonged room-temperature air exposure, such as storage, does not incorporate significant amounts of O into the CZTS absorbers. Nonetheless, the O partial pressure in air is about ten times higher compared to the O partial pressure in the ^{18}O anneals and hence the activation energies in Figure 5d could be underestimated as for ambient storage. Since O within few hundred nanometers from the surface cannot originate from the precursor, the Mo back contact, the SLG, or air exposure at less than 100 °C, the remaining possibility is that it arises from contaminations during the sulfurization or postsulfurization treatments. For example, during the sulfurization, a drop in sulfur partial pressure in the furnace has been previously observed,[54] indicating possible air leakage causing O contamination. Additionally, possible exchange between the SLG, which is close to temperatures where the glass starts to soften, and the atmosphere cannot be ruled out. These possible contamination sources are aggregated as the "Sulfurization step". **Figure 6** shows a

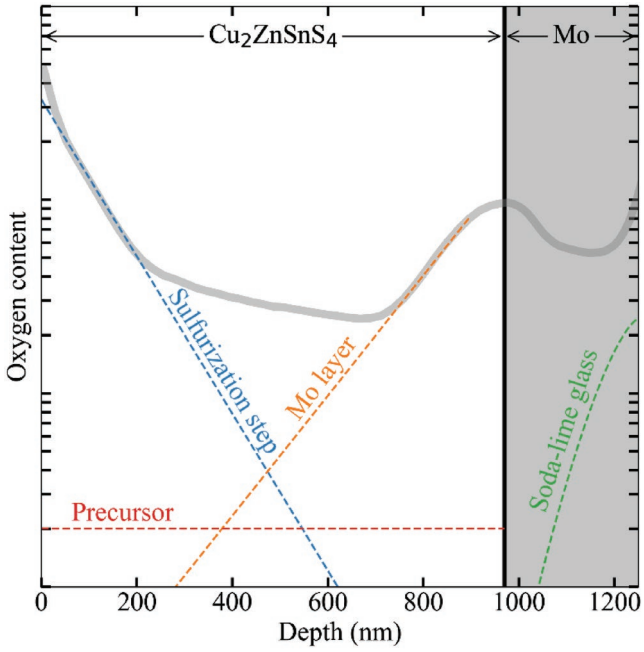

Figure 6. A representative O depth profile for a baseline processed CZTS absorber (gray thick line). The dashed lines illustrate a qualitative overview of oxygen sources contributing to the different parts of the depth profile based on the results from this work. Oxygen from the air exposure after processing should only contribute to the oxygen on the surface.

proposed assignment of the contributions to a typical O depth profile from a baseline processed CZTS absorber derived from the results given in Figure 5. The gray thick line represents the O depth profile for a baseline processed absorber ("Absorber untreated"), while the dashed lines illustrate a qualitative overview over which regions each oxygen source contributes mainly to. Based on the conducted analysis, we conclude that the sulfurization step and Mo layer account for the majority of O in the CZTS absorber. In addition, trace amounts of oxygen from the precursor may persist in the absorber as well. Conversely, O from the SLG does not diffuse sufficiently far to enter the CZTS layer during baseline processing. These results as such outline the strategies to tailor the O concentration in the kesterite absorbers.

2.3. Implications of O Incorporation and Trapping of Na

Based on the results presented in Sections 2.1 and 2.2, a deeper understanding of the mechanisms behind the correlation and the overall shape of the depth profiles for Na and O in Figure 1 can be deduced. The computed binding energy of 0.76 eV for Na—O complexes and the distinct ionic bonding nature evince that Na and O impurities in CZTS inevitably cluster together, whether it be in the bulk, surface, or grain boundary of the absorber. Na is known to be a fast diffuser in CIGS[15,55] and evidently CZTS,[10] where it promotes crystallization of the absorber layer.[56,57]

Consequently, the correlation between Na and O profiles observed in the kesterite absorbers can be explained by relatively slow O diffusion from the Mo back contact and the atmosphere during the sulfurization, as shown in Figure 6, and subsequently immobilizing the fast-diffusing Na via extensive formation of Na—O defect complexes. Hence, provided Na and O concentrations are of the same order, their depth profiles would appear correlated, as seen in Figure 1. Indeed, for "Precursor 400 °C", where the majority of the ^{18}O remained after the sulfurization, the depth profile exhibits an unusual but gradual increase in the total O concentration from the near-surface to the in-depth region of the sample (Figure S6, Supporting Information). Accordingly, for this sample, the Na and O profiles are also correlated throughout the sample, except for the CZTS/Mo interface region yields increased Na intensity.

Further, the proposed mechanism of O incorporation and interplay with Na can provide new insight into the Na redistribution occurring during postdeposition heat treatments. The Na distribution near the surface is likely to depend on the O_2 partial pressure in the atmosphere. Indeed in previous studies where postdeposition heat treatments were performed in N_2 atmosphere, the PCE was observed to reach a minimum between 100 and 200 °C and a maximum between 145 and 400 °C, with the optimum temperature depending on the N_2 pressure.[10,24,58] These temperatures are sufficient to cause extensive O incorporation in kesterite absorbers, as evident from our results shown in Figure 5c. Therefore, the change in PCE may also be influenced by in-diffusion of trace O from the atmosphere, in addition to the purely thermal effects emphasized in the original studies. As such, extensive care must be taken to tightly control O incorporation during the kesterite processing.

3. Conclusions

A general tendency for correlation and clustering between Na and O in kesterite absorbers formed by cosputtering was established by SIMS measurements. The atomistic mechanism behind the correlation was further explained using defect analyses within the DFT. A strong tendency for binding between Na and O impurities mediated by the strong ionic bonding was demonstrated. The computed total binding energies of 0.76 eV for NaO and 1.32 eV for Na_2O were proven to trigger formation of the nearest neighbor complexes of Na_{Cu} and O_S at all temperatures of baseline kesterite processing. The contributions from various O sources were evaluated by incorporation of the less abundant isotope ^{18}O at different stages of the CZTS baseline process. Based on these results, a model was proposed where the sulfurization step and the Mo layer are the main contributors of O in CZTS. Hence, the correlation between Na and O distributions can be explained by O immobilizing Na. Consequently, the redistribution of Na during postdeposition heat treatments of kesterites is strongly dependent on the availability of O. The observed interplay between Na and O in kesterite absorbers provides a foundation for more accurate impurity control needed for fabricating high-performance solar cell devices.

4. Experimental Section

The samples were processed through baseline processing steps for Cu_2ZnSnS_4 absorbers. Mo (99.97% purity) bilayer was DC sputtered

with Ar (99.9995% purity) as sputtering gas on top of soda-lime glass substrates. The bilayer consists of an adhesive layer sputtered at 2 Pa and a conductive layer sputtered at 0.8 Pa. CuS (99.99% purity), ZnS (99.99% purity), and SnS (99.99% purity) were cosputtered using a Lesker CMS-18 sputter system, with a 666 Pa Ar background pressure at a substrate temperature of 250 °C. Sulfurization was performed with 60–80 mg of sulfur in a pyrolytic carbon coated graphite box in a tube furnace at 550–580 °C for 13 min. The precursor compositions were determined with Rutherford backscattering-calibrated X-ray fluorescence measurements. At every step of the process, four pieces were taken out and annealed in an ^{18}O-rich atmosphere ([^{18}O]: 97.1%, [^{16}O]: 2.9% with 20 mbar pressure at room temperature). The cation ratios vary to a degree which could impact diffusion mechanisms. Nevertheless, for all four samples, each temperature series exhibits identical cation ratios. The samples were characterized with SIMS using a Cameca IMS 7*f* magnetic sector instrument. Cs^+ primary ions were utilized and both negative M^- and positive MCs^+ ions were detected, where "M" is the element of interest. Impact energies were 15 and 5 keV, respectively. The beam was rastered over an area of 150×150 μm^2 with a beam current of 20 nA. One sample was also measured with time-of-flight-energy elastic recoil detection analysis (ToF-E ERDA) with I^{8+} ions with 36 MeV primary energy to provide as a reference for SIMS calibration.[59,60] The depth was estimated by measuring the depth of each layer using a Dektak 8 Stylus profilometer. The first-principles calculations were carried out using the Vienna Ab initio Simulation Package (VASP).[61–63] The Perdew–Burke–Ernzerhof (PBE) functional[64] was employed to describe the exchange-correlation interaction and the projector augmented wave (PAW) pseudopotentials[65,66] were adopted to model the effect of core electrons. The pseudopotentials with Cu $3d^{10}4s^1$, Zn $3d^{10}4s^2$, Sn $4d^{10}5s^25p^2$, S $3s^23p^4$, O $2s^22p^4$, Li $2s^1$, Na $3s^1$, K $3p^64s^1$, Rb $4p^65s^1$, Cs $5s^25p^66s^1$, and Ag $4d^{10}5s^1$ valence electron configurations were chosen for the study. The cutoff energy threshold for the plane-wave basis was set to 350 eV. All the defect calculations were conducted on the orthorhombic CZTS supercell containing 64 atoms. The Brillouin-zone integrations were done on Γ-centered 4×4×4 Monkhorst–Pack grids.[67] Initial configurations for the defect pairs were created by placing Na at the equilibrium Cu site and O at the S equilibrium sites, followed by random perturbation of all atoms in the supercell. This approach yielded a total of 16 nonequivalent configurations for the considered defect pair, which accounts for Na substitution on both 2a and 2c Wyckoff sites in the kesterite CZTS. To optimize the defect geometries, the atomic relaxations were performed until reaching 0.01 eV Å^{-1} threshold for the Hellmann–Feynman forces. The charge transfer to the X atom was defined as $\Delta Q(X) = Q(X) - Q_{ref}(X)$, where $Q(X)$ and $Q_{ref}(X)$ are Bader charges on X atom in the systems containing the defect pair and the corresponding isolated defect, respectively. Importantly, since all except the interstitial defects were formed by substitution of isovalent elements, the first-principles investigation was constrained to the neutral supercell calculations. All the obtained DFT results were analyzed using Visualization for Electronic and Structural Analysis (VESTA)[68] and Python Materials Genomics (pymatgen).[69]

Supporting Information

Supporting Information is available from the Wiley Online Library or from the author.

Acknowledgements

This work was funded by the Research Council of Norway (Project No. 243642) and the Swedish Foundation for Strategic Research. The Research Council of Norway is also acknowledged for the support to the Norwegian Micro and Nano-Fabrication Facility, NorFab (Project No. 245963/F50). The authors acknowledge the Swedish National Infrastructure for Computing for providing access to supercomputer resources. S.G. would like to acknowledge J. K. Larsen, N. Saini, and S. Englund for assistance with sample preparation and processing, K. Rudisch for guidance on processing of ERDA data, and D. Primetzhofer for ERDA measurements. K.V.S. would like to thank O. I. Malyi and J. J. Scragg for the fruitful discussions of the results. X.L. and T.S.B. acknowledge funding from the Research Council of Norway ("SURKINOX" 258875) through the M-ERA.NET Joint Call 2016.

Conflict of Interest

The authors declare no conflict of interest.

Keywords

defect complexes, depth distributions, kesterite, oxygen, sodium

Received: March 5, 2019
Revised: April 30, 2019
Published online: June 4, 2019

[1] W. Wang, M. T. Winkler, O. Gunawan, T. Gokmen, T. K. Todorov, Y. Zhu, D. B. Mitzi, *Adv. Energy Mater.* **2014**, *4*, 1301465.
[2] S. G. Haass, M. Diethelm, M. Werner, B. Bissig, Y. E. Romanyuk, A. N. Tiwari, *Adv. Energy Mater.* **2015**, *5*, 1500712.
[3] K.-J. Yang, D.-H. Son, S.-J. Sung, J.-H. Sim, Y.-I. Kim, S.-N. Park, D.-H. Jeon, J. Kim, D.-K. Hwang, C.-W. Jeon, D. Nam, H. Cheong, J.-K. Kang, D.-H. Kim, *J. Mater. Chem. A* **2016**, *4*, 10151.
[4] S. Giraldo, M. Neuschitzer, T. Thersleff, S. López-Marino, Y. Sánchez, H. Xie, M. Colina, M. Placidi, P. Pistor, V. Izquierdo-Roca, K. Leifer, A. Pérez-Rodríguez, E. Saucedo, *Adv. Energy Mater.* **2015**, *5*, 1501070.
[5] T. Taskesen, J. Neerken, J. Schoneberg, D. Pareek, V. Steininger, J. Parisi, L. Gütay, *Adv. Energy Mater.* **2018**, *8*, 1703295.
[6] C. Yan, J. Huang, K. Sun, S. Johnston, Y. Zhang, H. Sun, A. Pu, M. He, F. Liu, K. Eder, L. Yang, J. M. Cairney, N. J. Ekins-Daukes, Z. Hameiri, J. A. Stride, S. Chen, M. A. Green, X. Hao, *Nat. Energy* **2018**, *3*, 764.
[7] A. Cabas-Vidani, S. G. Haass, C. Andres, R. Caballero, R. Figi, C. Schreiner, J. A. Márquez, C. Hages, T. Unold, D. Bleiner, A. N. Tiwari, Y. E. Romanyuk, *Adv. Energy Mater.* **2018**, *8*, 1801191.
[8] S. Giraldo, Z. Jehl, M. Placidi, V. Izquierdo-Roca, A. Pérez-Rodríguez, E. Saucedo, *Adv. Mater.* **2019**, *31*, 1806692.
[9] C. M. Sutter-Fella, J. A. Stückelberger, H. Hagendorfer, F. La Mattina, L. Kranz, S. Nishiwaki, A. R. Uhl, Y. E. Romanyuk, A. N. Tiwari, *Chem. Mater.* **2014**, *26*, 1420.
[10] H. Xie, S. López-Marino, T. Olar, Y. Sánchez, M. Neuschitzer, F. Oliva, S. Giraldo, V. Izquierdo-Roca, I. Lauermann, A. Pérez-Rodríguez, E. Saucedo, *ACS Appl. Mater. Interfaces* **2016**, *8*, 5017.
[11] Z.-K. Yuan, S. Chen, Y. Xie, J.-S. Park, H. Xiang, X.-G. Gong, S.-H. Wei, *Adv. Energy Mater.* **2016**, *6*, 1601191.
[12] T. Gershon, Y. S. Lee, R. Mankad, O. Gunawan, T. Gokmen, D. Bishop, B. McCandless, S. Guha, *Appl. Phys. Lett.* **2015**, *106*, 123905.
[13] T. Gershon, B. Shin, N. Bojarczuk, M. Hopstaken, D. B. Mitzi, S. Guha, *Adv. Energy Mater.* **2015**, *5*, 1400849.
[14] K. Sardashti, R. Haight, T. Gokmen, W. Wang, L.-Y. Chang, D. B. Mitzi, A. C. Kummel, *Adv. Energy Mater.* **2015**, *5*, 1402180.
[15] A. Laemmle, R. Würz, T. Schwarz, O. Cojocaru-Mirédin, P.-P. Choi, M. Powalla, *J. Appl. Phys.* **2014**, *115*, 154501.

[16] L. Kronik, D. Cahen, H. W. Schock, *Adv. Mater.* **1998**, *10*, 31.
[17] D. Cahen, R. Noufi, *Appl. Phys. Lett.* **1989**, *54*, 558.
[18] D. Cahen, R. Noufi, *Sol. Cells* **1991**, *30*, 53.
[19] D. W. Niles, M. Al-Jassim, K. Ramanathan, *J. Vac. Sci. Technol., A* **1999**, *17*, 291.
[20] Z. Su, K. Sun, Z. Han, H. Cui, F. Liu, Y. Lai, J. Li, X. Hao, Y. Liu, M. A. Green, *J. Mater. Chem. A* **2014**, *2*, 500.
[21] U. Rau, D. Braunger, R. Herberholz, H. W. Schock, J.-F. Guillemoles, L. Kronik, D. Cahen, *J. Appl. Phys.* **1999**, *86*, 497.
[22] J. K. Larsen, Y. Ren, N. Ross, E. Särhammar, S.-Y. Li, C. Platzer-Björkman, *Thin Solid Films* **2017**, *633*, 118.
[23] I. Repins, C. Beall, N. Vora, C. DeHart, D. Kuciauskas, P. Dippo, B. To, J. Mann, W.-C. Hsu, A. Goodrich, R. Noufi, *Sol. Energy Mater. Sol. Cells* **2012**, *101*, 154.
[24] D. Hironiwa, N. Sakai, T. Kato, H. Sugimoto, Z. Tang, J. Chantana, T. Minemoto, *Thin Solid Films* **2015**, *582*, 151.
[25] J. H. Kim, S.-Y. Choi, M. Choi, T. Gershon, Y. S. Lee, W. Wang, B. Shin, S.-Y. Chung, *Adv. Energy Mater.* **2016**, *6*, 1501902.
[26] R. V. Forest, E. Eser, B. E. McCandless, R. W. Birkmire, J. G. Chen, *AIChE J.* **2014**, *60*, 2365.
[27] N. Ross, S. Grini, K. Rudisch, L. Vines, C. Platzer-Bjorkman, *IEEE J. Photovoltaics* **2018**, *8*, 1132.
[28] R. Haight, X. Shao, W. Wang, D. B. Mitzi, *Appl. Phys. Lett.* **2014**, *104*, 033902.
[29] A. Rockett, J. S. Britt, T. Gillespie, C. Marshall, M. M. A. Jassim, F. Hasoon, R. Matson, B. Basol, *Thin Solid Films* **2000**, *372*, 212.
[30] T. Yamamoto, T. Watanabe, Y. Hamashoji, *Phys. B* **2001**, *308*, 1007.
[31] V. Probst, F. Karg, J. Rimmasch, W. Riedl, W. Stetter, H. Harms, O. Eibl, *MRS Proc.* **1996**, *426*, 165.
[32] T. Schwarz, O. Cojocaru-Mirédin, P. Choi, M. Mousel, A. Redinger, S. Siebentritt, D. Raabe, *Appl. Phys. Lett.* **2013**, *102*, 042101.
[33] O. Cojocaru-Mirédin, P.-P. Choi, D. Abou-Ras, S. S. Schmidt, R. Caballero, D. Raabe, *IEEE J. Photovoltaics* **2011**, *1*, 207.
[34] J. Keller, R. Schlesiger, I. Riedel, J. Parisi, G. Schmitz, A. Avellan, T. Dalibor, *Sol. Energy Mater. Sol. Cells* **2013**, *117*, 592.
[35] P. Schöppe, S. Schönherr, R. Würz, W. Wisniewski, G. Martínez-Criado, M. Ritzer, K. Ritter, C. Ronning, C. S. Schnohr, *Nano Energy* **2017**, *42*, 307.
[36] W.-J. Yin, Y. Wu, S.-H. Wei, R. Noufi, M. M. Al-Jassim, Y. Yan, *Adv. Energy Mater.* **2014**, *4*, 1300712.
[37] J. Li, D. B. Mitzi, V. B. Shenoy, *ACS Nano* **2011**, *5*, 8613.
[38] M. Wong, K. Tse, J. Zhu, *J. Phys. Chem. C* **2018**, *122*, 7759.
[39] C. Persson, A. Zunger, *Phys. Rev. Lett.* **2003**, *91*, 266401.
[40] C. Persson, A. Zunger, *Appl. Phys. Lett.* **2005**, *87*, 211904.
[41] Y. Yan, C.-S. Jiang, R. Noufi, S.-H. Wei, H. R. Moutinho, M. M. Al-Jassim, *Phys. Rev. Lett.* **2007**, *99*, 235504.
[42] S. Siebentritt, M. Igalson, C. Persson, S. Lany, *Prog. Photovoltaics* **2010**, *18*, 390.
[43] T. Maeda, A. Kawabata, T. Wada, *Phys. Status Solidi C* **2015**, *12*, 631.
[44] E. Ghorbani, J. Kiss, H. Mirhosseini, M. Schmidt, J. Windeln, T. D. Kühne, C. Felser, *J. Phys. Chem. C* **2016**, *120*, 2064.
[45] K. Tse, M. Wong, Y. Zhang, J. Zhang, M. Scarpulla, J. Zhu, *J. Appl. Phys.* **2018**, *124*, 165701.
[46] M. Han, X. Zhang, Z. Zeng, *Phys. Chem. Chem. Phys.* **2017**, *19*, 17799.
[47] L. E. Oikkonen, M. G. Ganchenkova, A. P. Seitsonen, R. M. Nieminen, *J. Appl. Phys.* **2013**, *114*, 083503.
[48] R. D. Shannon, *Acta Crystallogr., Sect. A: Found. Adv.* **1976**, *32*, 751.
[49] C. Tablero, *Thin Solid Films* **2012**, *520*, 5011.
[50] C. G. Van de Walle, J. Neugebauer, *J. Appl. Phys.* **2004**, *95*, 3851.
[51] H. Mehrer, A. W. Imre, E. Tanguep-Nijokep, *J. Phys.: Conf. Ser.* **2008**, *106*, 012001.
[52] N. P. Bansal, R. H. Doremus, *Handbook of Glass Properties*, Elsevier, Amsterdam **2013**.
[53] R. A. De Souza, J. A. Kilner, *Solid State Ionics* **1999**, 9.
[54] Y. Ren, N. Ross, J. K. Larsen, K. Rudisch, J. J. S. Scragg, C. Platzer-Björkman, *Chem. Mater.* **2017**, *29*, 3713.
[55] R. V. Forest, B. E. McCandless, X. He, A. A. Rockett, E. Eser, K. D. Dobson, R. W. Birkmire, *J. Appl. Phys.* **2017**, *121*, 245102.
[56] S. Grini, N. Ross, C. Persson, C. Platzer-Björkman, L. Vines, *Thin Solid Films* **2018**, *665*, 159.
[57] N. Ross, J. Larsen, S. Grini, L. Vines, C. Platzer-Björkman, *Thin Solid Films* **2017**, *623*, 110.
[58] T. Ericson, F. Larsson, T. Törndahl, C. Frisk, J. Larsen, V. Kosyak, C. Hägglund, S. Li, C. Platzer-Björkman, *Sol. RRL* **2017**, *1*, 1700001.
[59] S. Englund, V. Paneta, D. Primetzhofer, Y. Ren, O. Donzel-Gargand, J. K. Larsen, J. Scragg, C. Platzer-Björkman, *Thin Solid Films* **2017**, *639*, 91.
[60] M. S. Janson, *Contes Conversion of Time-Energy Spectra: A Program for ERDA Data Analysis*, Internal Report, Uppsala University, Uppsala, **2004**.
[61] G. Kresse, J. Furthmüller, *Comput. Mater. Sci.* **1996**, *6*, 15.
[62] G. Kresse, J. Hafner, *Phys. Rev. B* **1993**, *47*, 558.
[63] G. Kresse, J. Furthmüller, *Phys. Rev. B* **1996**, *54*, 11169.
[64] J. P. Perdew, K. Burke, M. Ernzerhof, *Phys. Rev. Lett.* **1996**, *77*, 3865.
[65] P. E. Blöchl, *Phys. Rev. B* **1994**, *50*, 17953.
[66] G. Kresse, D. Joubert, *Phys. Rev. B* **1999**, *59*, 1758.
[67] H. J. Monkhorst, J. D. Pack, *Phys. Rev. B* **1976**, *13*, 5188.
[68] K. Momma, F. Izumi, *J. Appl. Crystallogr.* **2011**, *44*, 1272.
[69] S. P. Ong, W. D. Richards, A. Jain, G. Hautier, M. Kocher, S. Cholia, D. Gunter, V. L. Chevrier, K. A. Persson, G. Ceder, *Comput. Mater. Sci.* **2013**, *68*, 314.